Journal Pre-proof

A moment-of-fluid method for resolving filamentary structures using a symmetric multi-material approach

Philippe Hergibo, Timothy N. Phillips and Zhihua Xie

Please cite this article as: P. Hergibo, T.N. Phillips and Z. Xie, A moment-of-fluid method for resolving filamentary structures using a symmetric multi-material approach, *Journal of Computational Physics*, 112401, doi: https://doi.org/10.1016/j.jcp.2023.112401.

This is a PDF file of an article that has undergone enhancements after acceptance, such as the addition of a cover page and metadata, and formatting for readability, but it is not yet the definitive version of record. This version will undergo additional copyediting, typesetting and review before it is published in its final form, but we are providing this version to give early visibility of the article. Please note that, during the production process, errors may be discovered which could affect the content, and all legal disclaimers that apply to the journal pertain.
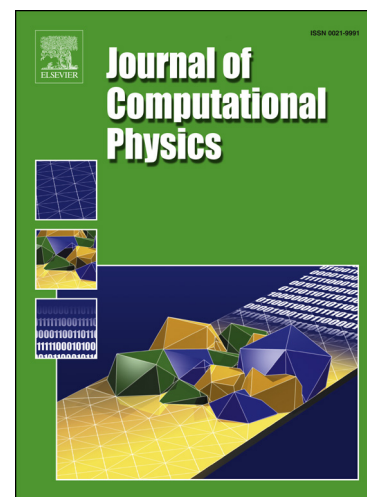
Highlights

- Symmetric filament reconstruction.
- A new optimisation algorithm is proposed based on the bisection method.
- Validated with various benchmarks with high-order convergence and high accuracy.
- Lagrangian advection approach is used without CFL restriction.

A moment-of-fluid method for resolving filamentary structures using a symmetric multi-material approach

Philippe Hergibo[a,b], Timothy N. Phillips[b], Zhihua Xie[a,*]

[a]*School of Engineering, Cardiff University, Queen's Buildings, Cardiff, CF24 3AA, UK*
[b]*School of Mathematics, Cardiff University, Abacws, Cardiff, CF24 4AG, UK*

Abstract

Multiphase flows have implications in many areas of engineering. The moment-of-fluid (MOF) method is an interface capturing method using both volume fraction and centroid within a cell for interface reconstruction. A symmetric approach to reconstruct thin structures is presented. Also called filaments, these subcell characteristics involve multi-material reconstruction. In addition, a new optimisation algorithm is presented using a bisection method without any necessary initial condition. Using a Lagrangian approach for dynamic cases, no restrictions are imposed on timestep. The new method is validated using several benchmark cases that have been studied extensively in the literature. A near quadratic order of convergence and high accuracy is achieved while maintaining an acceptable runtime.

*Corresponding author. Email: zxie@cardiff.ac.uk; Tel.: +44(0)29-20879375.

1. Introduction

²¹   Multiphase flow modelling is crucial in several real-life examples such as ²² wave breaking, water splashing or bubbles. It is also important in industrial ²³ applications from oil-and-gas transportation to inkjet printing. Its modelling ²⁴ requires an accurate representation of the interface between two or more ²⁵ fluids. In addition, it is challenging to resolve thin filaments during the ²⁶ breakup process.

²⁷   Several techniques for representing interfaces have been developed over ²⁸ the years [1]. These fall into two broad categories: interface tracking and in- ²⁹ terface capturing. Interface tracking aims to track a set of points representing ³⁰ the interface using the associated velocity field [2, 3, 4, 5]. Its robustness and ³¹ simplicity of implementation makes it easily accessible. However, this may ³² not be the case when there is a large deformation of the interface.

³³   The level set method is an example of an interface capturing technique. ³⁴ This method uses a smooth function to describe the sharp interface [6]. The ³⁵ zero level set of the function defines the interface. The accuracy and robust- ³⁶ ness makes it useful for complex multiphase flows, yet in most engineering ³⁷ problems, the lack of mass conservation of this technique makes it undesir- ³⁸ able. Improvements have been made on this issue using a conservative level ³⁹ set method [7, 8], which has also been extended recently for non-Newtonian ⁴⁰ multiphase flows [9]. Another interface capturing technique is the volume- ⁴¹ of-fluid (VOF) method which was initially developed by Hirt and Nichols ⁴² [10]. The interface, either horizontal or vertical known as Simple Line Inter- ⁴³ face Calculation (SLIC), is defined by the volume fraction of surrounding grid ⁴⁴ cells. In a subsequent development, Young's method introduced an improved ⁴⁵ orientation to the interface known as Piecewise Linear Interface Construction ⁴⁶ (PLIC) [11]. Both VOF methods are subject to natural diffusion and artifi- ⁴⁷ cial surface tension causing the separation of forming filaments and exhibit ⁴⁸ large errors. In addition, only one interface is able to be reconstructed in a ⁴⁹ cell, which means that structures thinner than a cell size cannot be resolved. ⁵⁰ More sophisticated VOF approaches have been developed using a parabolic ⁵¹ reconstruction [12, 13] or trying to resolve filaments [14]. Methods coupling ⁵² the level set and VOF methods have also been developed [15].

⁵³   The latest advancement in the evolution of the VOF method is the ⁵⁴ moment-of-fluid (MOF) method. The MOF method uses both the volume ⁵⁵ fraction and its centroid to reconstruct the interface thereby increasing the ⁵⁶ accuracy in interface orientation. The error in interface reconstruction is im-

proved when compared to a standard VOF method and the MOF method possesses superior mesh convergence properties. The MOF method is able to reconstruct a piecewise linear interface without using information from neighbouring cells. In addition, MOF can be implemented with ease for general polyhedral cells. However, MOF can be time-consuming as the computational bottleneck is an optimisation algorithm which is required in order to reconstruct the interface in each cell.

The initial MOF method was presented in 2005 using an optimisation algorithm [16]. While conserving mass in each cell, the best approximation is to find the normal to the interface that minimises the distance between the reference and reconstructed centroid. In a subsequent development, an analytical solution which avoids the need to employ an optimisation algorithm was found by Lemoine et al. [17]. However, this is restricted to rectangular cells. Further work has been performed with the MOF method using more complex approaches. Multi-material reconstruction is facilitated when three or more materials are present [18, 19], under-resolved filaments allowing thin structure reconstruction [20], symmetric reconstruction [21] and even adaptive mesh refinement [22]. Attempts have also been made to couple the level set method with the MOF method [23, 24]. Due to its expensive computational cost, further improvements have been made only for Cartesian cells using pre-computed values to find the reconstructed centroid in an efficient manner [25] and even a machine learning approach [26] improving drastically the runtime. When large deformations of the interface occur, standard MOF techniques are not precise enough to maintain a *smooth* interface and breakup occurs similar to VOF methods. To overcome the problem of unphysical breakup, we propose a novel symmetric multi-material approach to maintain the morphology of the interface for under-resolved filamentary structures. By combining the advantages of each approach, we construct a more precise interface at maximum deformation while maintaining an acceptable runtime. The optimisation algorithm uses a bisection method that does not require any parameter tuning. Capturing and reconstructing the exact topology yields time-consuming computation which has been simplified in our model. The novelty of the proposed method and the difference between the filament and standard MOF methods are highlighted in Fig. 1. A new test is presented to highlight large deformation of thin interfacial structures.

The paper is structured as follows. In Section 2, the standard MOF and its advection approach are described detailing the choice of using a bisection method in the optimisation part. Then, the filamentary method is
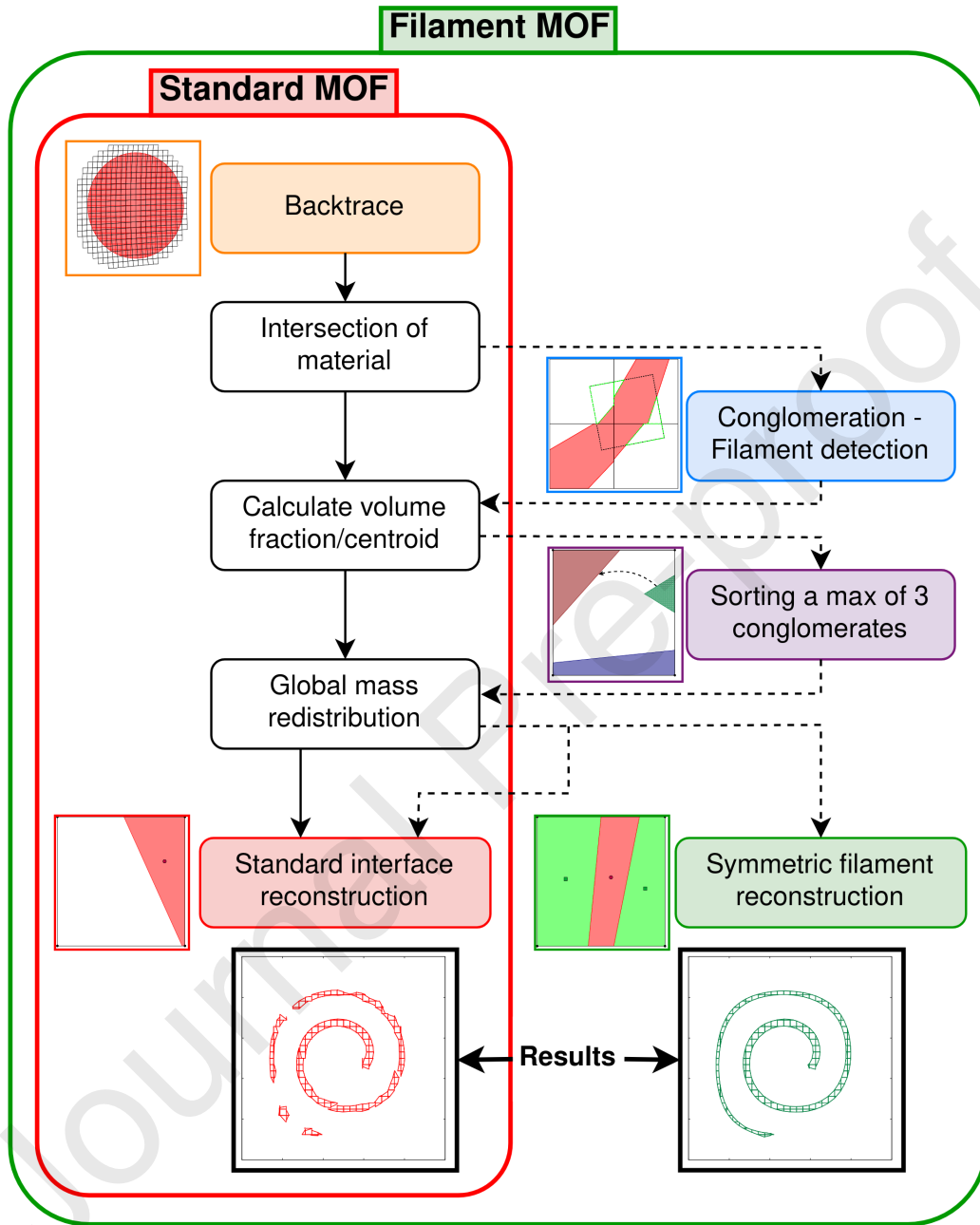
3

Figure 1: Flowchart highlighting the key steps for a filament MOF method compared to a standard MOF method

95 presented in Section 3. The conglomeration algorithm and adjacency test
96 are described, as well as the choice of capping the number of materials at
97 three. Finally, Section 4 presents and analyses the results for many advec-
98 tion benchmark problems to demonstrate the accuracy and advantages of the
99 proposed method. Some concluding remarks are given in Section 5.

100 ## 2. MOF method

101 *2.1. Interface reconstruction*

102 *2.1.1. Problem definition*

103 Let us define the problem imposed by the MOF method in order to re-
104 construct an interface. Consider a convex polygon ω that is defined by n
105 vertices, $\mathbf{x}_1$,..., $\mathbf{x}_n$. The area of ω, denoted $|\omega|$, and the centroid (centre of
106 mass), denoted $\mathbf{x}_c(\omega)$ can be computed as follows

$$|\omega| = \frac{1}{2} \sum_{i=1}^{n} \left[\mathbf{x}_i \times \mathbf{x}_{i+1} \right] \tag{1}$$

$$\mathbf{x}_c(\omega) = \frac{1}{6 |\omega|} \sum_{i=1}^{n} \left[\mathbf{x}_i \times \mathbf{x}_{i+1} \right] \left(\mathbf{x}_i + \mathbf{x}_{i+1} \right) \tag{2}$$

107 Note that $\mathbf{x}_{n+1} = \mathbf{x}_1$. Let Ω depict an arbitrary convex cell, hence not
108 restricted to a Cartesian cell, filled with two different materials. Only con-
109 sidering the first material μ_1, its area relative to the area of the cell is denoted
110 by $F_{ref}(\mu_1)$ which corresponds to the volume fraction. Similarly, $\mathbf{x}_{ref}(\mu_1)$ is
111 defined to be the reference centroid of μ_1 within the cell.
112 The MOF reconstruction problem is formulated as an optimisation prob-
113 lem in which the distance between the reference centroid $\mathbf{x}_{ref}(\mu_1)$ and the
114 reconstructed centroid $\mathbf{x}_{act}(\mu_1)$ is minimised while keeping the volume frac-
115 tion of the reconstructed polygon $F_{act}(\mu_1)$ equal to the volume fraction of μ_1.
116 One can summarise the optimisation problem as follows:

$$\begin{cases} min \, |\mathbf{x}_{ref}(\mu_1) - \mathbf{x}_{act}(\mu_1)| \\ F_{ref}(\mu_1) = F_{act}(\mu_1) \end{cases} \tag{3}$$

117 If μ_1 already occupies a polygon with a piecewise linear interface, the
118 MOF method aims to reconstruct the exact interface. As shown in Fig. 2,
119 the reference interface may be curved, hence the minimised centroid distance
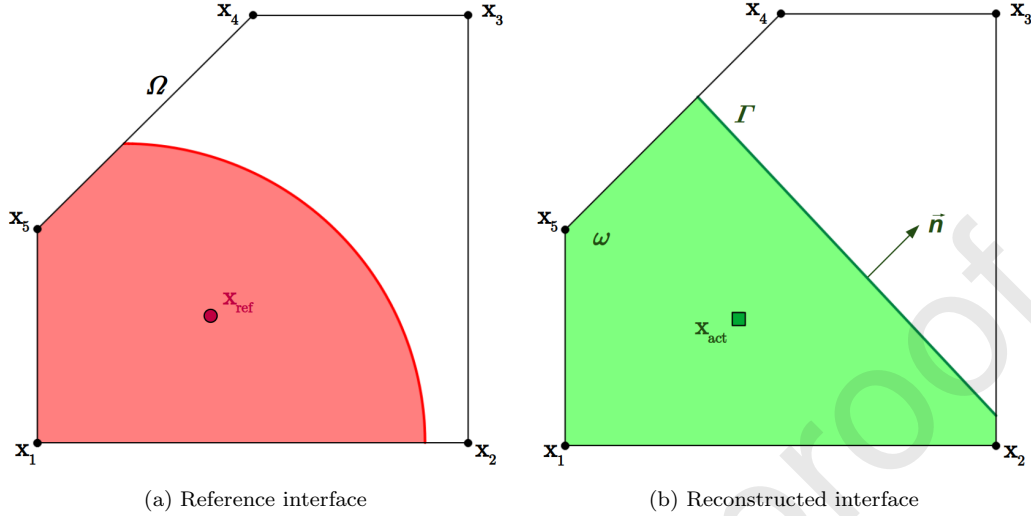120 will aim to give the *best* reconstruction.

5

(a) Reference interface (b) Reconstructed interface

Figure 2: Reference vs. reconstructed interface with their respective centroids $\mathbf{x}_{ref}$ and $\mathbf{x}_{act}$. $\mathbf{n}$ denotes the reconstructed normal to the interface. Γ denotes the length of the interface segment.

2.1.2. Reconstruction

The reconstructed normal to the interface within a polygon can be evaluated analytically [17] but only for rectangular cells. However, for cells of any other geometrical shape, a minimisation algorithm is needed to evaluate the normal to the interface. The unit normal is defined to be $\mathbf{n} = [\cos(\phi), \sin(\phi)]$ where ϕ corresponds to the angle the interface makes with the horizontal. To cover all possible normals, $\phi \in [0, 2\pi]$. The minimisation function, also known as the objective function, is recalled $f(\phi) = |\mathbf{x}_{act}(\phi) - \mathbf{x}_{ref}|$. In general, $f(\phi)$ may have multiple local minima. The first derivative of the objective function for a convex cell, initially given in [16], is defined by

$$f'(\phi) = 2((\mathbf{x}_{act}(\phi) - \mathbf{x}_{ref}) \cdot \mathbf{x}'_{act}(\phi)) \tag{4}$$

where $\mathbf{x}'_{act}(\phi)$ is given by

$$\mathbf{x}'_{act}(\phi) = \frac{1}{12} \frac{|\Gamma(\phi)|^3}{|\Omega| \, F_{ref}(\mu_1)} [-\sin(\phi), \cos(\phi)] \tag{5}$$

and is evaluated using the length of the reconstructed interface segment $\Gamma(\phi)$.

6

133 *2.1.3. Bisection method*

134   In this section, a new algorithm is presented to evaluate the normal to the
135 interface. The algorithm used in this paper to find the global minimum is a
136 bisection method. Using four quadrants, explicitly $[0, \pi/2]$, $[\pi/2, \pi]$, $[\pi, 3\pi/4]$
137 and $[3\pi/4, 2\pi]$, the zeros of the first derivative of the objective function can be
138 determined. The bisection method uses only a maximum of 10 iterations per
139 quadrant to find the local minimum with a tolerance of 10^{-10}. When the value
140 of the first derivative falls below the specified tolerance at the boundaries of
141 a quadrant, the bisection method is terminated for that quadrant. Once the
142 minimum for each quadrant is found, evaluating the objective function for all
143 valid values will give the global minimum. The global minimum of $f(\phi)$ will
144 result in the best approximation for the optimisation problem defined above.
145 Fig. 3 shows the set of solutions as well as the objective function within the
146 four quadrants. Knowledge of the normal enables one to flood the cell [17] to
147 reconstruct the interface with the minimum distance between the reference
148 and reconstructed centroid, which is defined as the least centroid error.

149   This method has the advantage of not requiring any initial condition and
150 fine parameter tuning to converge to the solution and is guaranteed to find
151 the global minimum. However it may require a larger number of iterations
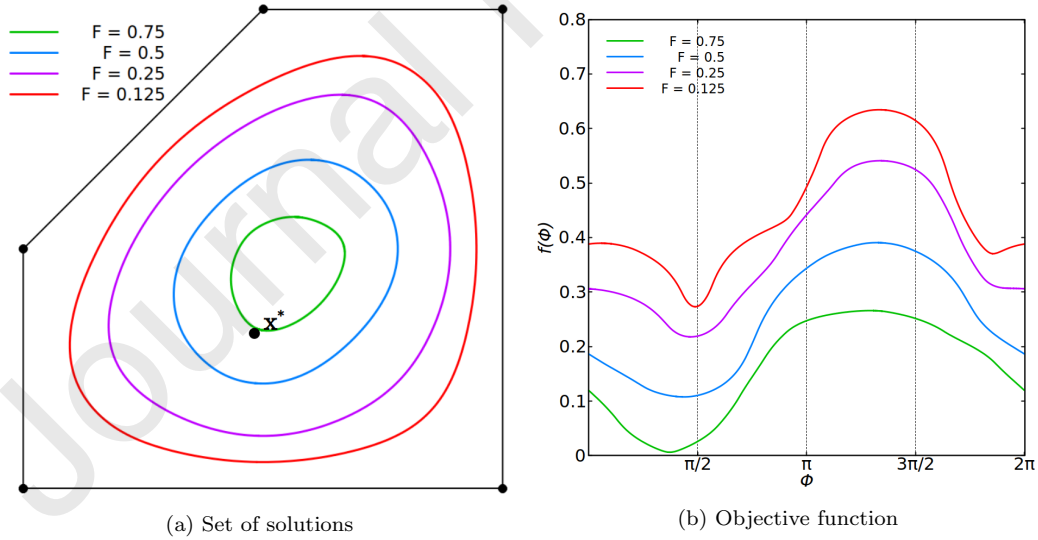152 to converge.

(a) Set of solutions

(b) Objective function

Figure 3: Set of solution and objective function for various volume fractions $F = 0.125$, 0.25, 0.5 and 0.75. $\mathbf{x}^*$ denotes the reference centroid.

2.2. Advection

Dynamic tests involve advecting materials across multiple time iterations. Information from the previous time step is needed in order to reconstruct the material interface at the next time step. The most natural way to perform this reconstruction is to use a Lagrangian pre-image to capture the volume fraction and centroid of a material.

All vertices of a cell are advected backwards in time using a 2nd-order Runge-Kutta scheme to form the backtrace cell as seen in Fig. 4a. The backtrace cell may intersect several cells at the previous time level. The Sutherland-Hodgman polygon clipping algorithm is used in order to intersect each of these cells to gain information about volume fraction and centroid. The advantage of using the Lagrangian approach is that there is no limitation on the CFL number used in the model. Moreover, the Lagrangian advection procedure is said to be unsplit, which means it only requires one advection and reconstruction per cell [27].

2.2.1. Advection of volume fraction

To compute the volume fraction at the next time step, the sum of intersecting areas form the new volume fraction of the cell as highlighted in purple in Fig. 4b. However, in some cases, its value may depend on the backtrace cell area relative to the cell area. If the backtrace cell area is larger than the cell area, there is potential for the volume fraction to exceed unity. On the contrary, if the backtrace cell area is smaller than the cell area, there is potential for the volume fraction to be smaller than unity while being entirely filled with one material. These cases may occur when the backtrace cell intersects with only one material, making the new theoretical volume fraction equal to unity but the actual volume fraction is either greater than or less than unity. If this is the case, a post advection remapping procedure is introduced in order to ensure that the total material mass is consistent throughout the advection time. The difference between the actual volume fraction and unity are gathered, then redistributed equally across all cells that can accept a gain or loss of mass/volume fraction. This is defined as a global redistribution [28]. The modified mass in each cell is negligible so that the shape of the interface is not changed significantly, which has been demonstrated later in the validation. To be less expensive, this procedure is only performed once per time step, which means there is a risk of not being able to redistribute the total mass.

8

2.2.2. Advection of centroid

To compute the centroid at the next time step, the centroid of the intersection of the backtrace cell with a cell is computed, then advected using the same scheme as for the backtrace cell advection as shown in Fig. 4c. All cell intersection centroids are advected forward in time individually. The new reference centroid is obtained by weighting the cell intersection centroids with their volume fraction. Since all centroids are framed within the backtrace cell at the previous time step, the new reference centroid is guaranteed to be within the cell after forward advection.

(a) Lagrangian backtrace   (b) Volume intersection   (c) Centroid advection
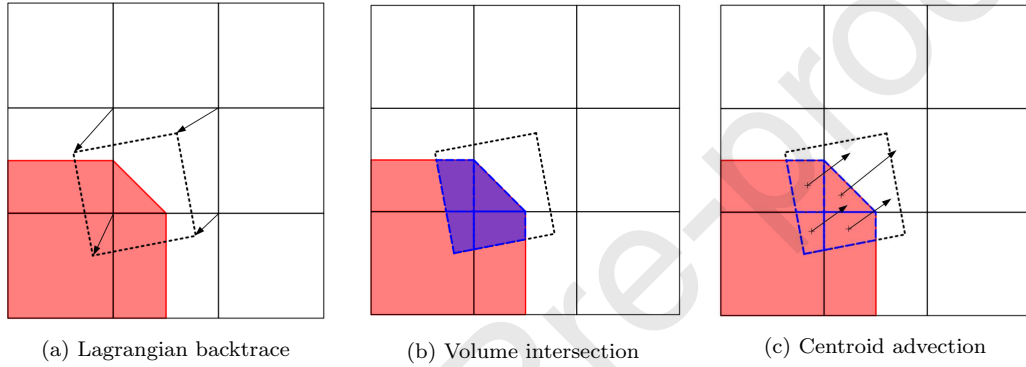
Figure 4: Dynamic test: advection of backtrace cell backwards, intersection of volumes, advection of centroids individually

3. Filament capturing

Filaments are defined as thin strands of material surrounded by another material within a cell. These are structures thinner than a cell size. A standard MOF reconstruction would create a linear interface splitting the cell in two, hence not reconstructing the topology correctly as shown in Fig. 5. When considering a filament, two linear interfaces emerge, one on each side of the structure, meaning that two reconstructions are needed to capture the topology perfectly. In filament reconstruction, the conglomeration algorithm is capable of detecting polygons of the same material that are not adjacent by using the numerical adjacency condition. A fictitious material is introduced to reconstruct one of the polygons surrounding the filament. Once reconstructed, the fictitious material is reassigned to its original material. A symmetric multi-material reconstruction is presented to generate a better topology.

9

(a) Reference interface   (b) Standard reconstruction   (c) Filament reconstruction

Figure 5: Schematic diagrams showing (a) a reference interface, (b) the standard MOF reconstruction and (c) filament MOF reconstruction.

3.1. Conglomeration

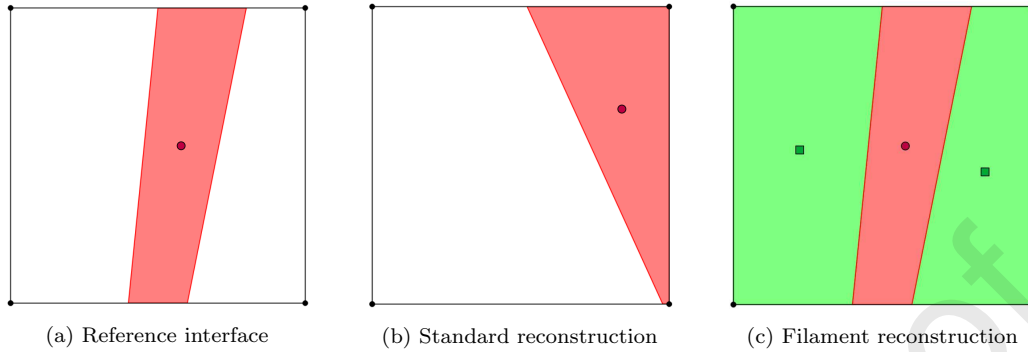Filament reconstruction is performed when some adjacent polygons forming one material, called a conglomerate, are not adjacent to other conglomerates of the same material. The conglomeration algorithm allows us to identify whether a cell needs a multi-material reconstruction or a standard reconstruction. It is possible to identify all polygons of one material intersecting with the backtrace cell as shown in Fig. 6. Once all of these polygons are gathered, the conglomeration algorithm tests if each of these polygons are adjacent to each other. Conglomerates are considered even when they do not split a cell, i.e. being only adjacent to one cell edge. The green conglomerate in Fig. 8b is one of these. Flotsam are not discussed in this paper, in general on a coarse mesh they do not tend to exist. If more than one conglomerate is found, then one of these conglomerates is considered to be the fictitious material. The conglomeration algorithm is a tree-based structure testing adjacency of a list of polygons until the lowest level does not find any adjacent polygons. Alg. 1 details the procedure to identify conglomerates. The reference volume fraction and reference centroid can easily be computed.

3.2. Adjacency

The adjacency test is performed on all sides (segments) of a polygon with respect to another polygon. Some tolerance is accepted as sides may not be perfectly adjacent but can still be considered adjacent. For the purpose of numerical round-off errors, each segment is described by a vector and if the magnitude of the cross-product of two vectors meets the lower bound of a tolerance, here $\Delta x \Delta y \epsilon$ with $\epsilon = 10^{-3}$, then segments are considered parallel.

10

Algorithm 1 Conglomeration algorithm

Initialise list of polygons *list_poly*
while *list_poly* **do**
  new_group ← *list_poly(1)*
  while *iter* **do**
    for $k = 1, \text{size}(list\_poly)$ **do**
      if *is_adjacent(new_group(), list_poly(k))* **then**
        Remove *list_poly(k)*
        Add *list_poly(k)* to *new_group()*
        iter ← **true**
      end if
    end for
  end while
end while
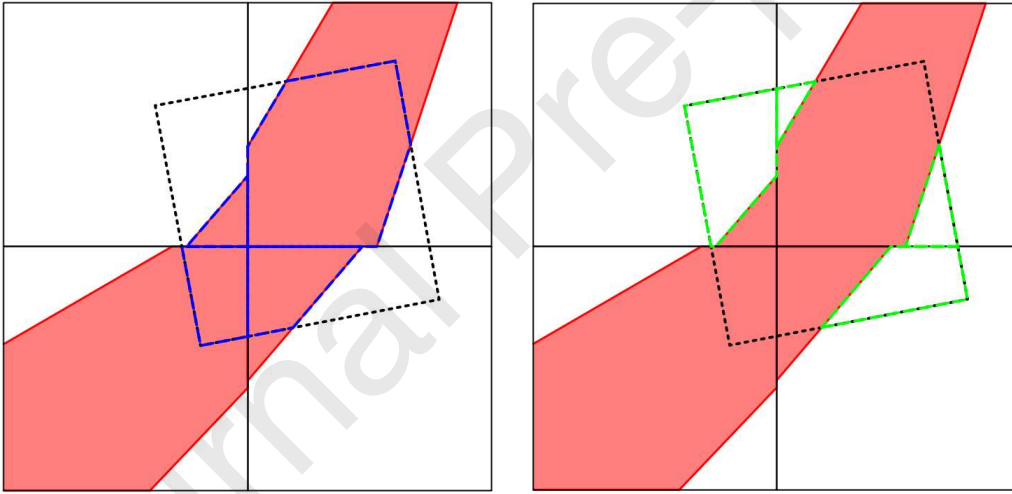
(a) Intersection and conglomeration of material μ_1 (b) Intersection and conglomeration of material μ_0

Figure 6: Conglomeration of polygons within the backtrace cell (dashed black outline) leading to the creation of a fictious material for a 3-material reconstruction. (a) Material μ_1 has 1 conglomerate (outline in blue); (b) Material μ_0 has 2 conglomerates (outline in green)

Segments may be considered parallel, yet they also need to be adjacent. Hence, the endpoint of a segment is projected onto the line defined by the other segment. If the distance between the endpoint of the segment and its

11

²³⁹ projection falls below the specified tolerance, here $\Delta x\epsilon$, the projection of an
²⁴⁰ endpoint also needs to fall between the bounds of the other segment. Only if
²⁴¹ all conditions are satisfied, both polygons are considered to be adjacent and
²⁴² hence form a conglomerate. Alg. 2 summarise the conditional procedure to
²⁴³ test if two polygons are adjacent with three nested conditions. Fig. 7 shows
²⁴⁴ two polygons within a cell. Segments are highlighted in order to indicate
²⁴⁵ the process of evaluating parallel and adjacent segments from two distinct
²⁴⁶ polygons. Condition 1 is represented with gold segments. Condition 1 and
²⁴⁷ 2 are represented with blue segments. All three conditions are represented
²⁴⁸ with red segments.

Algorithm 2 Adjacency test

  Initialise *vector_poly1, vector_poly2* **based on all** *vertex_l1, vertex_l2*
  for l2 = 1, size(*vector_poly2*) **do**
    for l1 = 1, size(*vector_poly1*) **do**
      {% Condition 1}
      if abs(cross_product(*vector_poly2(l2)*,*vector_poly1(l1)*)) $\leq \Delta x \cdot \Delta y \cdot \epsilon$
  then
        {% Condition 2}
        if distance(*vertex_l2*, projection_on_line(*vertex_l2, line(vector_poly1)*)) $\leq$
  $\Delta x \cdot \epsilon$ **then**
          {% Condition 3}
          if projection_on_segment(*vertex_l2, segment_l1*) $\leftarrow$ **true then**
            is_adjacent $\leftarrow$ **true**
          end if
        end if
      end if
    end for
  end for

---

²⁴⁹ *3.3. Limitation to three materials*

²⁵⁰   It may happen that more than three conglomerates form within the back-
²⁵¹ trace cell. In that case, a multi-material reconstruction can be considered.
²⁵² However, it can lead to expensive reconstruction when testing all the com-
²⁵³ binations for several cells per iteration. For this purpose, the number of
²⁵⁴ conglomerates is capped at three in our model. Conglomerates are sorted by
²⁵⁵ their volume fraction.

12

(a) Parallel segments but not adjacent
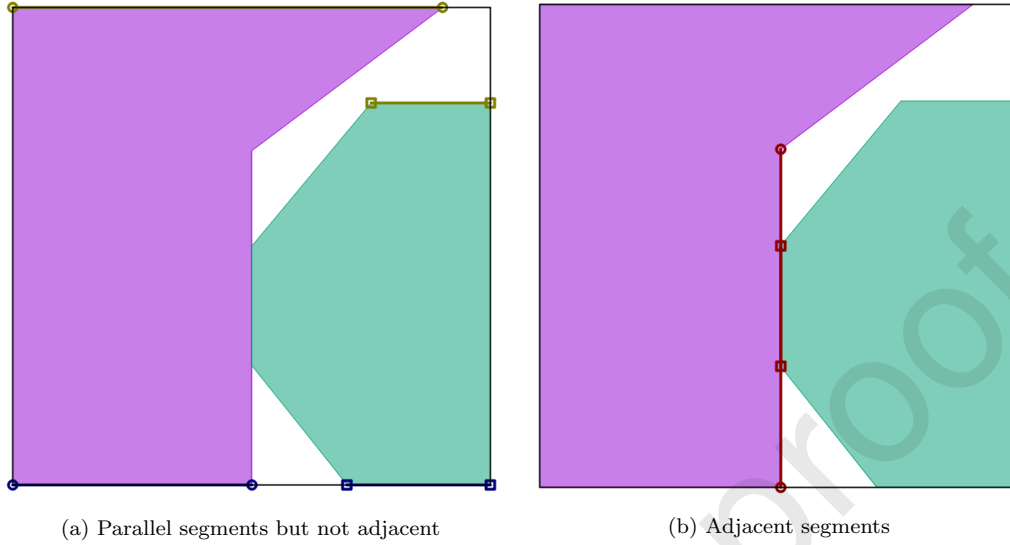
(b) Adjacent segments

Figure 7: Schematic diagrams to test adjacent segments with another polygon: (a) shows two configurations where segments are parallel. Projection of the endpoints do not fall within tolerance (highlighted in gold). One of the projections of the endpoints does not fall within the other segment (highlighted in blue); (b) shows two segments that are parallel and adjacent, the projection of the endpoints falls within tolerance and within the other segment.

If two conglomerates exist for each material, the following condition is tested. If the second conglomerate of one of the materials has a volume fraction smaller than 10^{-3}, then its volume fraction is added to the main (largest in volume fraction) conglomerate. If there still exists two conglomerates for each material, no conglomerates are considered and a standard reconstruction with the total volume fraction per material is performed. Fig. 8a highlights this scenario. Indeed, coloured conglomerates belong to Material 2, explicitly 2 and 2'. Material 1 also have two conglomerates in white, explicitly 1 and 1'. None of them are smaller than 10^{-3} in volume fraction.

In other cases, conglomerates with the smallest volume are "reattached" to the largest conglomerate of the same material in the cell, usually where one material has one conglomerate and the other has more than two conglomerates. Then, these smaller conglomerates have their volume fraction added to the largest conglomerates. Fig. 8b highlights this scenario. Three conglomerates (colored) belong to Material 2, here explicitly 2, 2' and 2''. Conglomerate 2'' will be reattached to Conglomerate 2, while Conglomerate

13

272 $2'$ will be considered to be the fictitious material for reconstruction. "Reat-
273 taching" to the nearest conglomerates based on the distance between their
274 respective centroids may also be considered but does not affect the topology
275 greatly as volume fraction for these conglomerates is often very small.
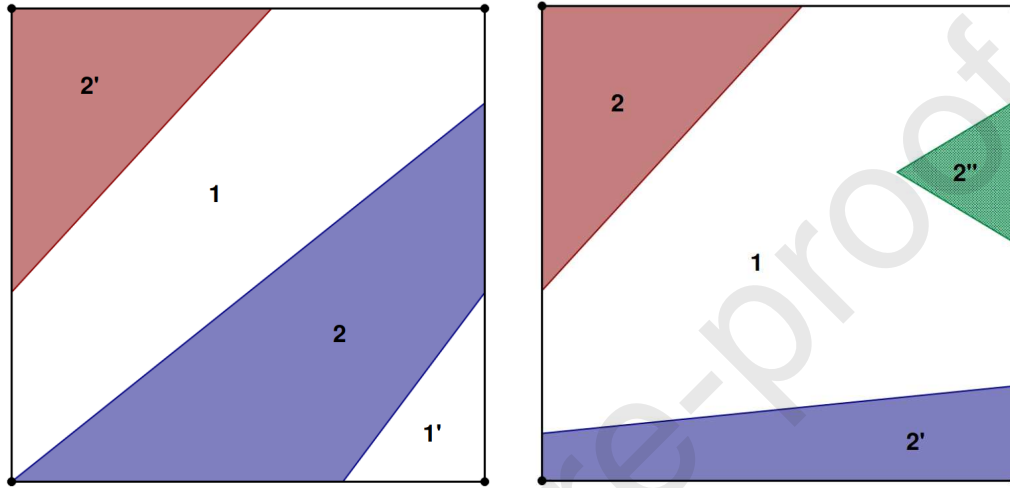
(a) Two conglomerates exist of size larger than 10^{-3} for each material leading to them being reconstructed as a standard MOF

(b) Three conglomerates exist for Material 2 leading to reattachement of the green conglomerate to the red (largest in cell)

Figure 8: Schematic showing two complex examples of sorting multiple conglomerates within the same cell. We assume all colored polygons belong to Material 2.

276 *3.4. Symmetric reconstruction of filaments*

277   The reason to cap the number of materials at three is based on com-
278 putational cost. Reconstructing more than three materials at once has a
279 significantly higher cost than only three materials. In addition, using a sym-
280 metric reconstruction of filaments may provide a better topology in material
281 reconstruction.

282   A standard reconstruction aims to reconstruct an interface based only on
283 minimising the centroid error of one material regardless of the other material
284 in cell reconstruction. In some cases, this can lead to a large error in the
285 remaining material centroid. The symmetric reconstruction approach aims
286 to minimise both centroids at the same time. The objective function $f_{sym}(\mathbf{n})$,
287 combining both centroid defects, is given by

14

$$f_{sym}(\mathbf{n}) = |\mathbf{x}_{ref}(\mu_1) - \mathbf{x}_{act}(\mu_1)(\mathbf{n})| + |\mathbf{x}_{ref}(\mu_{rem}) - \mathbf{x}_{act}(\mu_{rem})(\mathbf{n})| \qquad (6)$$

288 where $x_{ref}(\mu_{rem})$ denotes the reference centroid of the remaining material in
289 cell, and $x_{act}(\mu_{rem})$ is its reconstruction centroid.

290   When it comes to filament reconstruction or three material reconstruc-
291 tion, the standard approach is to test all ordering combinations and evaluate
292 the topology that reduces the total centroid defect. This procedure is called
293 a sequential reconstruction. The total centroid defect E can be expressed as
294 the sum of all material μ_i centroid errors

$$E = \sqrt{\sum_i^n |\mathbf{x}_{ref}(\mu_i) - \mathbf{x}_{act}(\mu_i)|^2} \qquad (7)$$

295   Consider three materials A, B and C, then six different configurations are
296 possible. Explicitly, and in order of reconstruction, these are (ABC), (ACB),
297 (BAC), (BCA), (CAB) and (CBA). A symmetric reconstruction reduces the
298 number of combinations to only three, thereby reducing the computational
299 effort. Considering the same materials, (ABC) and (ACB) would be redun-
300 dant as the first reconstruction minimises A and the grouping of B and C.
301 Then, (BC) or (CB) will result in the same reconstruction as only symmetric
302 reconstruction is considered. As seen in Fig. 9, a symmetric reconstruction
303 provides a *better* topology.

304   4. Results

305   In this section, several benchmark problems are considered with the aim
306 of testing the performance of the new filament MOF method. Several prob-
307 lems are of considerable interest since the associated velocity field yields high
308 deformation in the material. Maintaining the correct topology at maximum
309 deformation is attractive and important for most engineering problems. How-
310 ever, in order to assess the predictive capability of interface capturing meth-
311 ods, each of the flows is reversed over the same time period and compared
312 to its original configuration. Whilst comparison with the initial condition is
313 possible, the MOF enables one to evaluate the difference between the final
314 reconstruction and the original/reference configuration rather than the initial
315 reconstruction. From a computational cost perspective, our model uses an

15

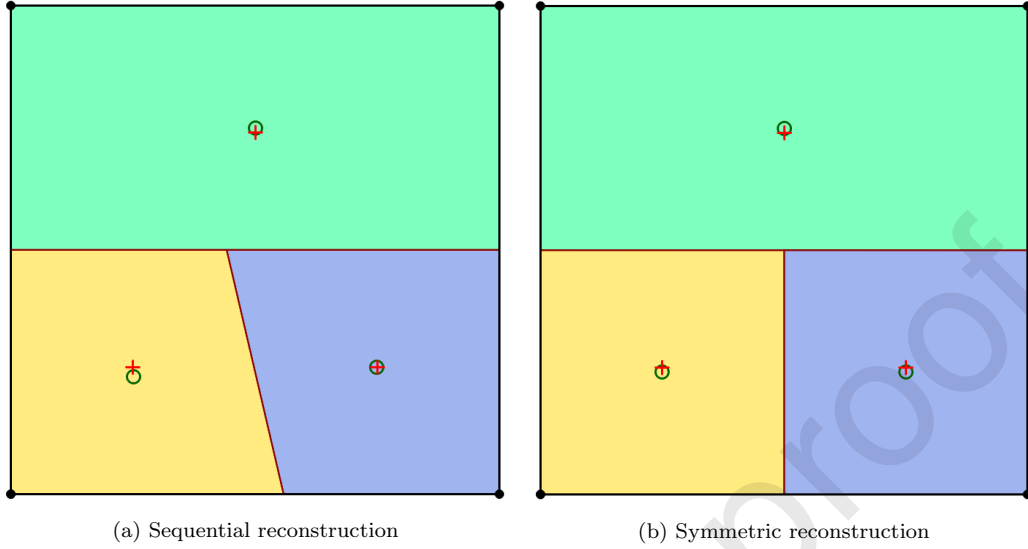(a) Sequential reconstruction   (b) Symmetric reconstruction

Figure 9: Comparison of (a) sequential and (b) symmetric reconstruction when using three materials, where (+) denotes the reference centroids and (o) denotes the reconstructed centroids.

³¹⁶ analytical reconstruction where possible. Indeed, when only the reconstruc-
³¹⁷ tion of a piecewise linear interface between two materials in a Cartesian cell
³¹⁸ is required, this approach is significantly more efficient. In order to reduce
³¹⁹ the total error in reconstruction, the interface is reconstructed based on the
³²⁰ material with the smallest volume fraction in a cell as suggested by Makun-
³²¹ dan et al. [24]. For cases involving more than two materials reconstruction,
³²² the symmetric multi-material approach is chosen.

³²³ *4.1. Error evaluation*

³²⁴   Evaluating errors in interface reconstruction is a powerful tool to com-
³²⁵ pare different interface tracking/capturing methods. The numerical errors in
³²⁶ terms of volume fraction can be evaluated with the L_1 error norm E_{L_1} as

$$E_{L_1} = \sum |F_{final} - F_{initial}| \, |\Omega| \tag{8}$$

³²⁷ its relative error norm E_r

$$E_r = \frac{\sum |F_{final} - F_{initial}| \, |\Omega|}{\sum |F_{initial}| \, |\Omega|} \tag{9}$$

16

328 and its maximum error norm L_∞

$$L_\infty = \max_i |F_{final} - F_{initial}| \, |\Omega| \tag{10}$$

329   A more representative error measure is the symmetric difference error
330 which provides a better estimate of the interface reconstruction error. The
331 symmetric difference error E_{sym} is given by

$$E_{sym} = \sum \left| \omega^{ref} \cup \omega^{act} - \omega^{ref} \cap \omega^{act} \right| \tag{11}$$

332   When comparing the reference interface with its reconstruction in indi-
333 vidual cells, the symmetric difference error can be interpreted as the area
334 between the two interfaces. Fig. 10 shows three different scenarios of in-
335 tersecting interfaces and highlights the area corresponding to the symmetric
336 difference error E_{sym}. Some simple calculations are necessary to evaluate the
337 area of a segment.
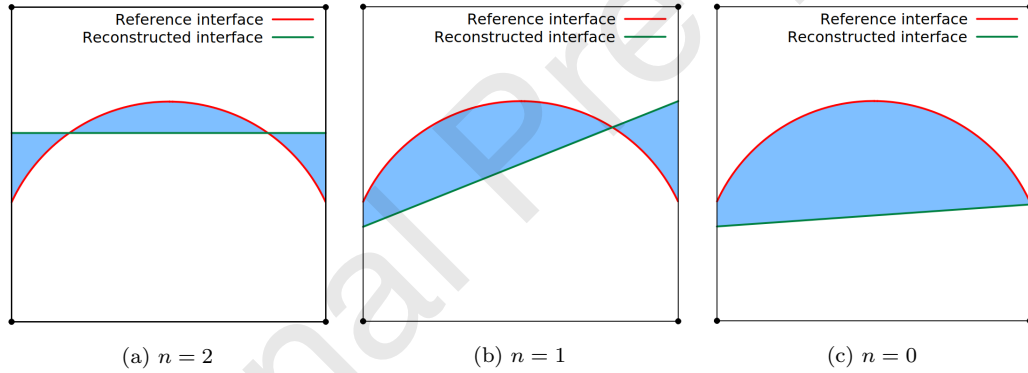
(a) $n = 2$ (b) $n = 1$ (c) $n = 0$

Figure 10: Symmetric difference error E_{sym} in a single cell. The area shaded in blue highlights the error corresponding to E_{sym} irrespective of the number of times, n, the reconstructed interface intersects the reference interface: (a) $n = 2$, (b) $n = 1$, (c) $n = 0$.

338   As well as evaluating the error in reconstruction, ensuring mass conser-
339 vation is also crucial during these advection tests. In 2D, mass conservation
340 corresponds to area preservation and mass loss is given by the expression

$$\Delta m = \sum |F_{final}| \, |\Omega| - \sum |F_{initial}| \, |\Omega| \tag{12}$$

341

342

17

343 *4.2. Benchmark: Zalesak slotted disc*

344   In this benchmark test case, a slotted disk is advected in a rigid body
345 rotation motion. A circle of radius $r = 0.15$, with a slotted rectangle of width
346 $w = 0.05$ and a maximum height of $h = 0.85$, is centered at $(0.5, 0.75)$ in a
347 unit domain. The corresponding velocity field is given by

$$\mathbf{u}(x, y) = \begin{bmatrix} 0.5 - y \\ x - 0.5 \end{bmatrix} \tag{13}$$

348

349

350   This case does not exhibit any filament formation, however it shows that
351 the conglomeration algorithm works for velocity fields that are rotating rather
352 than deforming the interface. Five different uniform grids have been used
353 explicity 32×32, 64×64, 128×128, 256×256 and 512×512. On the
354 coarsest mesh is 32×32, the number of iterations is set to be $n_{it} = 1256$
355 and $\Delta t = 2\pi/n_{it}$. The number of iterations is increased proportionally with
356 increasing mesh refinement. Hence, Δt is decreased correspondingly.
357   In order to study the error convergence, the error calculation for this test
358 case is based on the L_1 error. Table 1 summarises the L_1 error for different
359 mesh sizes and highlights the convergence of the numerical approximation.
360 In addition, Fig. 11 highlights the final solution after a full body rotation
361 for the first three grids. The shape of the original interface is captured well.
362 However, the sharp edges around the slotted rectangle have been smoothed
363 out during the rotation. Indeed, the MOF method is not able to capture these
364 edges regardless of the degree of mesh resolution. The maximum error L_∞ is
365 a more relevant measure of the error for this problem in order to understand
366 the order of convergence around sharp edges. In this case, second order
367 convergence may be attained in some instances but it may depend on the
368 alignment of the sharp edges of the slotted disk with the grid.
369   The behaviour of the L_1 error over one rotation is shown in Fig. 12 for
370 three different meshes mentioned in Fig. 11. The plot highlights that despite
371 the interface only rotating, the error increases during the rotation progresses
372 as the interface reconstruction error accumulates at each time step.

373 *4.3. Benchmark: Reversible Vortex T=8*

374   The reversible vortex is a benchmark test case for deforming advection
375 cases. A circle of radius $r = 0.15$ centered at $[0.5, 0.75]$ in a unit domain is

18

Table 1: Dependence of the L_1 error, E_{L_1}, relative error, E_r, and maximum error L_∞ on mesh size for the Zalesak slotted disc problem

Mesh size	E_{L_1}	E_r	L_∞
32	$3.17 \times 10^{-3}(-)$	$5.45 \times 10^{-2}(-)$	2.77×10^{-4} (-)
64	$9.02 \times 10^{-4}(1.81)$	$1.55 \times 10^{-2}(1.81)$	5.23×10^{-5} (2.40)
128	$3.81 \times 10^{-4}(1.24)$	$6.54 \times 10^{-3}(1.24)$	3.47×10^{-5} (0.59)
256	$1.35 \times 10^{-4}(1.50)$	$2.31 \times 10^{-3}(1.50)$	1.52×10^{-5} (1.19)
512	$4.93 \times 10^{-5}(1.45)$	$8.47 \times 10^{-4}(1.45)$	2.47×10^{-6} (2.62)

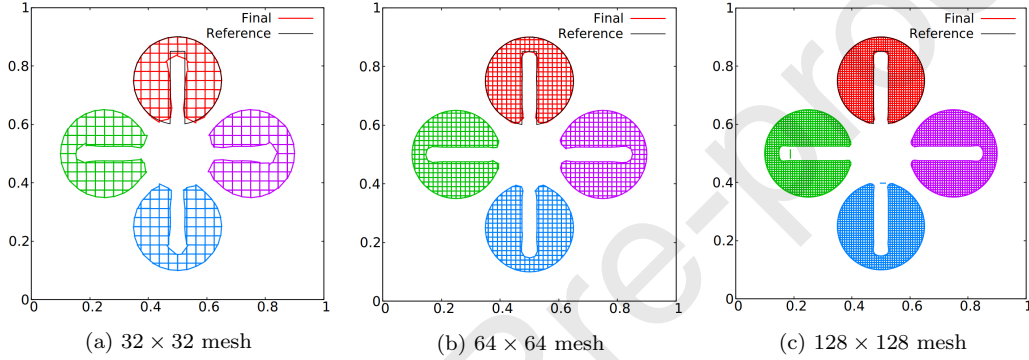(a) 32×32 mesh   (b) 64×64 mesh   (c) 128×128 mesh

Figure 11: Solution of rigid body rotation for the Zalesak slotted disc. Green depicts a quarter of rotation. Blue half rotation. Purple three quarter of rotation. Red depicts a full rotation and final solution. The black outline depicts the reference interface.

deformed in a divergence-free velocity field given by

$$\mathbf{u}(x,y,t) = \begin{bmatrix} -\sin^2(\pi x)\sin(2\pi y) \\ \sin^2(\pi y)\sin(2\pi x) \end{bmatrix} \cos(\pi t/T) \tag{14}$$

where T represents the full period and $T/2$ the time at maximum deformation. Here $T = 8$. The Courant-Friedrichs-Lewy (CFL) number is 1, hence the number of iterations $n_{it} = 256$ and $\Delta t = \Delta x$ when a 32×32 uniform Cartesian mesh is considered. The number of iterations increases proportionally with the mesh.

The circle deforms in a filamentary structure at maximum deformation $t = T/2$. For this test case, filament detection is enabled. Several grids from 32×32 to 1024×1024 have been used to perform this dynamic test case.

The symmetric difference error, E_{sym}, is shown in Table 2 for the initial reconstruction and at the final stage. The performance of our method is
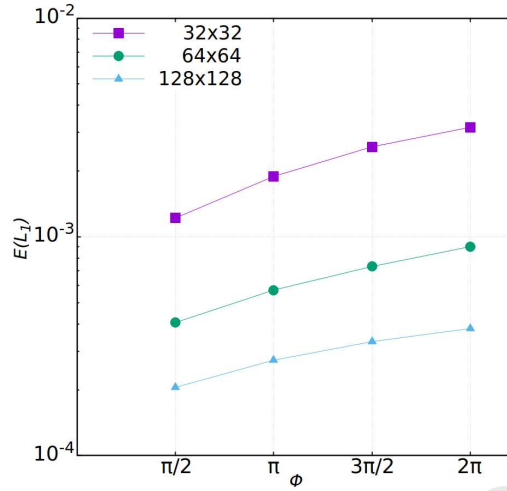
19

Figure 12: Behaviour of the L_1 error during the rigid body rotation of the Zalesak slotted disc for different mesh sizes. Φ denotes the angle of full body rotation.

compared with the results obtained using other MOF methods as well as with the standard MOF. Runtime, rounded to the next integer value, is also compared because the MOF method can be computationally expensive. Currently, the code has not been parallelised and so the computations are performed on a single core. The order of convergence of this method is also highlighted as well as the mass difference.

Fig. 13 shows the maximum deformation before reversal and the final reconstruction for different mesh sizes: 32×32, 64×64 and 128×128, respectively. Using a filament approach, the vortex does not exhibit any spurious separated structures, even on a coarse mesh. In this test case, the trailing tail shows a thicker structure as the coarse cell cannot reconstruct the filament tail accurately. As the mesh is refined, the tail becomes well-defined but thicker than the filament width. The MOF method naturally creates these structures as it exhibits some cross-stream diffusion, leading to a shorter tail than expected. The symmetric difference error converges slightly faster than other MOF methods with a smaller error on the finest mesh. Runtime is also considerably faster by a factor of between two to five. The error shows high order of convergence, almost matching the reference order two. The symmetric difference error for standard MOF exhibits a slower order of convergence on coarser grids. However, the symmetric difference error is almost indistinguishable on the finest meshes for the two approaches.

20

Table 2: Reversible vortex test case data using $T = 8$ compared with the standard MOF (STD MOF) and with results generated using other MOF methods in the literature: a standard MOF with adaptive mesh refinement (AMR) method [22], a filament AMR method [20], a coupled level-set MOF (CLSMOF) [24].

Mesh size	32	64	128	256	512	1024
E_{sym} in [22]	2.34×10^{-2}	3.31×10^{-3}	5.78×10^{-4}	1.22×10^{-4}	2.01×10^{-5}	-
Order of convergence	-	2.82	2.51	2.24	2.60	-
E_{sym} in [20]	3.12×10^{-3}	6.91×10^{-4}	2.77×10^{-4}	-	-	-
Order of convergence	-	2.17	1.31	-	-	-
Runtime in [20]	32.6	200	635.3	-	-	-
E_{sym} in [24]	1.32×10^{-3}	1.01×10^{-3}	5.44×10^{-4}	2.76×10^{-4}	1.38×10^{-4}	6.90×10^{-5}
Order of convergence	-	0.39	0.89	0.98	1.0	1.0
E_{sym} for STD MOF	1.42×10^{-2}	7.46×10^{-3}	1.29×10^{-3}	9.19×10^{-5}	1.45×10^{-5}	4.07×10^{-6}
Order of convergence	-	0.92	2.53	3.81	2.66	1.83
Initial E_{sym}	1.74×10^{-4}	4.06×10^{-5}	1.28×10^{-5}	2.99×10^{-6}	1.49×10^{-7}	4.19×10^{-8}
Final E_{sym}	2.80×10^{-3}	5.06×10^{-4}	1.54×10^{-4}	4.45×10^{-5}	1.48×10^{-5}	3.64×10^{-6}
Order of convergence	-	2.46	1.71	1.79	1.58	2.02
Mass difference	1.09×10^{-6}	2.54×10^{-7}	3.98×10^{-8}	2.31×10^{-9}	-1.50×10^{-6}	2.05×10^{-12}
Runtime (s)	17	31	95	447	4856	43942

4.3.1. Influence of the mass redistribution

The remapping procedure does not affect the topology greatly as the volume fraction that needs to be redistributed during the procedure is very small. Indeed, during the deformation of the vortex the volume fraction redistributed oscillates between 10^{-4} and 10^{-10}. During the early stages of the deformation, most mass has to be redistributed as there are many cells in the inner part of the circle that are over/under-filled and very few cells are mixed cells, i.e. cells containing an interface. On the contrary, at maximum deformation, very few cells are over/under-filled cells, most of them contains an interface, or two in the case of filaments. Fig. 14 summarises this. The difference between with and without the post advection remapping procedure is highlighted in Fig. 14a, whereas Fig. 14b shows the variation of volume fraction redistributed per iteration. Note that the mass is redistributed equally between mixed cells. Tab. 3 shows the mass difference for the reversible vortex case ($T = 8$) for a case where the mass was redistributed and when it was not. Two orders of magnitude of difference can be observed, which shows the advantage of the proposed method for mass
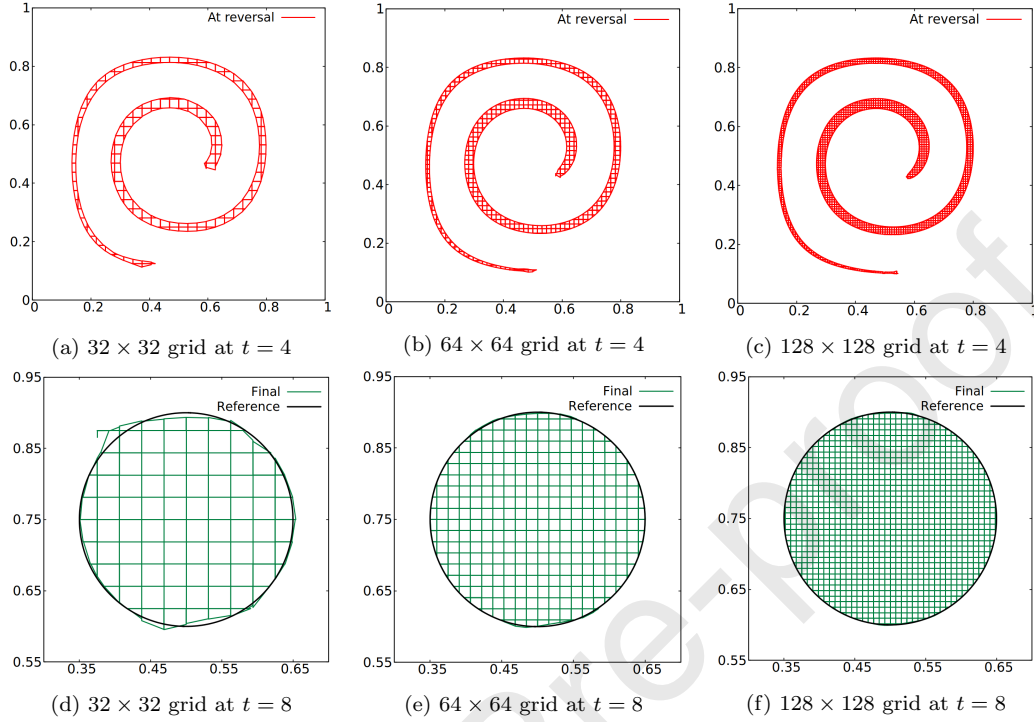
21

Figure 13: Reversible vortex test case using $T = 8$ for 32×32, 64×64 and 128×128 grids. Top row of figures shows the maximum deformation. Bottom row of figures shows the final interface.

425 conservation.

4.3.2. Influence of the CFL number on the interface

427 One expects the CFL number to influence the interface reconstruction.
428 However, the Lagrangian advection procedure is not greatly affected by the
429 CFL number. Therefore, most cases are performed with the maximum avail-
430 able CFL number which equals unity. In theory, a CFL number greater than
431 unity can be used for such advection benchmarks. However, the stencil used
432 in the dynamic test procedure encompasses only a 3×3 stencil and therefore
433 limits larger CFL numbers. Fig. 15 shows a zoom on the final reconstruction
434 for different CFL numbers 0.2, 0.4, 0.5, 0.8 and 1.0 and the error convergence.
435 A lower CFL number will induce a larger number of iterations, therefore in-
436 creasing the chances of error in reconstruction. However, the difference in
437 error is relatively small in magnitude. The difference on the interface only

22
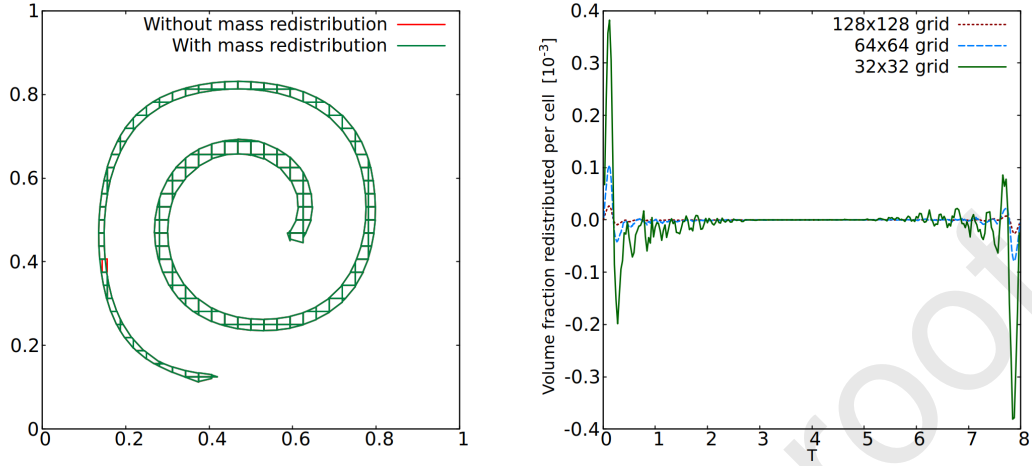
(a) Filament MOF reconstruction including comparison with post advection remapping procedure

(b) Volume fraction redistributed as a function of the time period of the reversible vortex T

Figure 14: Comparison showing the effect on the interface shape of the post advection remapping procedure for mass conservation and the actual mass redistributed per iteration for different grids.

occurs near the top of the circle which is near the tip of the filament at maximum deformation.

4.3.3. Influence of the filament capable method

Filament capable MOF is able to reconstruct a moving interface with a greater accuracy and better topology. Indeed, under strong deformations, materials tend to break up when they are not predicted to do so. At the instant of maximum deformation, a continuous interface is more likely and will result in better modelling of multiphase flows. Fig. 16 highlights both visual reconstruction and convergence of the standard and filament solution. Fig. 16a shows that several break ups of the dynamic interface occur when a standard MOF reconstruction is implemented. The final reconstruction does not match the reference circle. Fig. 16b compares the order of convergence between a standard and the proposed filament approach, together with other MOF methods. Note that for the finer grids, the error tends to the same values as the thickness of the structure is larger than a cell size, hence not using the filamentary approach as frequently during the dynamic test.

23

Table 3: Mass difference for the reversible vortex with and without post advection remapping procedure

Mesh size	With redistribution	Without redistribution
32	1.09×10^{-6}	1.35×10^{-4}
64	2.54×10^{-7}	2.58×10^{-5}
128	3.98×10^{-8}	3.75×10^{-6}
256	2.31×10^{-9}	5.72×10^{-6}

(a) Zoom on final reconstruction on a 64×64 grid

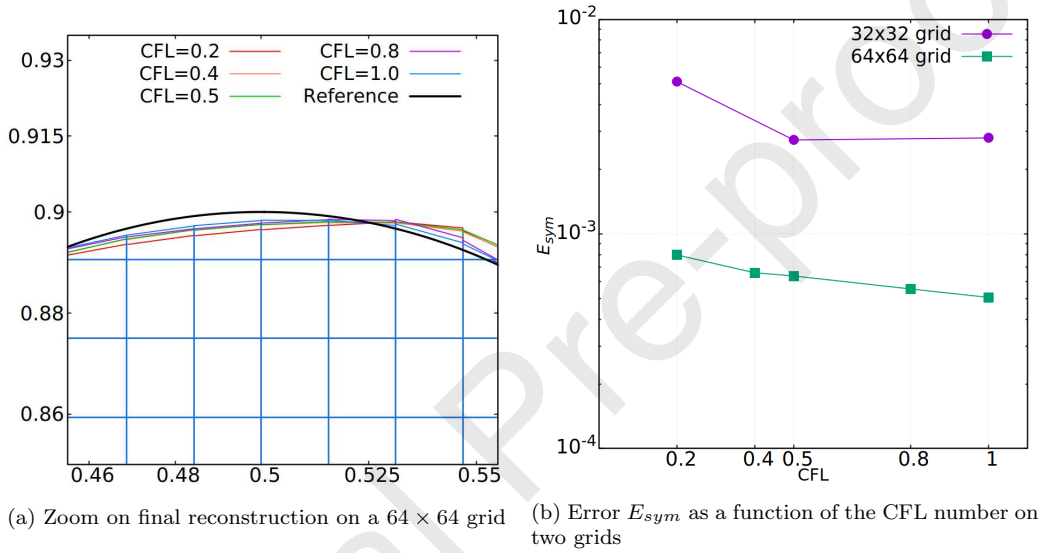(b) Error E_{sym} as a function of the CFL number on two grids

Figure 15: (a) Influence of the CFL number on the final reconstruction of part of the interface; (b) symmetric difference error, E_{sym}, as a function of the CFL number for two grids: 32×32 and 64×64

4.4. Test case: Reversible Vortex T=12

This is the same benchmark test case as considered in Section 4.3 except that the full period is increased to $T = 12$. A larger period increases the deformation and thinner filaments are exhibited. Table 4 summarises the symmetric difference error for six different mesh sizes from 32×32 to 1024×1024. As the material is more deformed than in the previous benchmark with $T = 8$, the expected symmetric difference error is larger. As the mesh is refined, there are no longer significant benefits associated with using the filament method as the thickness of the deformed filament is greater than a cell width. Consequently, the order of convergence decreases from quadratic

24
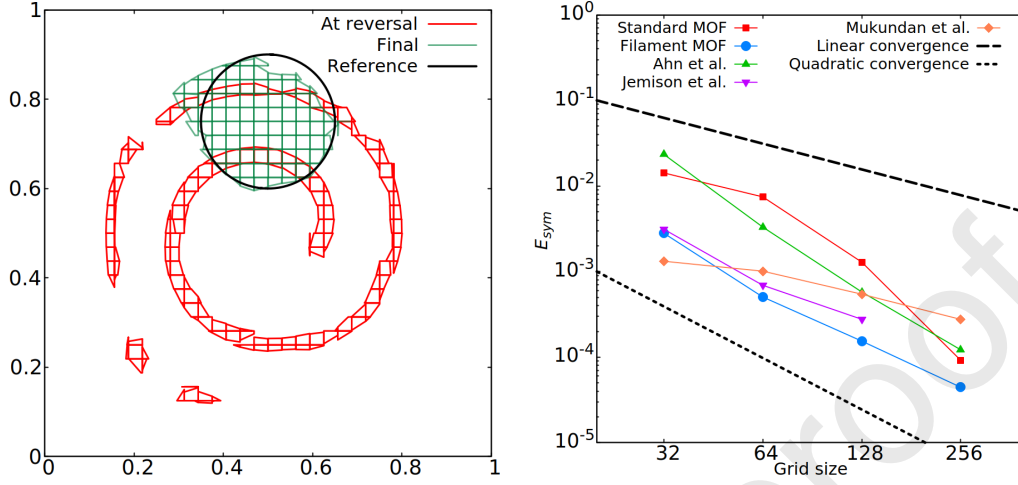
(a) Standard MOF reconstruction for a 32×32 grid at reversal (in red) and final (in green). Black outline denotes the reference interface.

(b) Convergence Behaviour of the standard MOF and filament MOF compared with the literature using E_{sym}.

Figure 16: (a) Influence of the filament capable method on the reconstruction; (b) Symmetric difference error E_{sym} compared with other MOF methods. Convergence rate is compared with a linear and quadratic reference.

to linear until the order of convergence of the filament MOF follows that for standard MOF. The mass difference is very comparable. However, runtime is increased significantly. Indeed, the number of cells containing a filament structure compared to a standard interface is very large. Fig. 17 highlights the morphology of the very thin interface. Because filament reconstruction is computationally more expensive, the runtime is increased by a factor of three.

4.5. Benchmark: Droplet flow

The droplet flow test case has a nonlinear divergence free velocity field. The deformation of material tears an initial circle of radius $r = 0.125$ centred in a unit domain into a V-shape. The velocity field is given by

$$\mathbf{u}(x,y,t) = \begin{bmatrix} 0.125(8x-4) \\ 0.125\left[-(8y-4) - 4 - (1-(8x-4)^2 - (8x-4)^4)\right] \end{bmatrix} f(t) \quad (15)$$

The velocity field is a function of time as the amplitude, $f(t)$, varies in time according to

25

Table 4: Symmetric difference error, L_1 error, mass difference and runtime for the reversible vortex test case using $T = 12$ and its comparison with the standard MOF (STD MOF).

Mesh size	32	64	128	256	512	1024
Final E_{sym}	4.98×10^{-3}	9.91×10^{-4}	2.48×10^{-4}	1.27×10^{-4}	2.06×10^{-5}	6.33×10^{-6}
Order of convergence	-	2.32	1.99	0.96	2.62	1.70
$E(L_1)$	4.18×10^{-3}	9.62×10^{-4}	2.58×10^{-4}	1.23×10^{-4}	4.11×10^{-5}	6.29×10^{-6}
Order of convergence	-	2.11	1.89	1.06	1.58	2.70
Mass difference	3.12×10^{-6}	3.08×10^{-7}	4.93×10^{-8}	4.01×10^{-9}	-8.93×10^{-12}	-7.33×10^{-7}
Runtime (s)	51	95	180	958	7334	65418
E_{sym} for STD MOF	2.66×10^{-2}	1.81×10^{-2}	3.37×10^{-3}	1.18×10^{-3}	4.05×10^{-5}	7.70×10^{-6}
Order of convergence	-	0.55	2.42	1.51	4.86	2.39

(a) 32×32 grid at $t = 6$ (b) 64×64 grid at $t = 6$ (c) 128×128 grid at $t = 6$

(d) 32×32 grid at $t = 12$ (e) 64×64 grid at $t = 12$ (f) 128×128 grid at $t = 12$
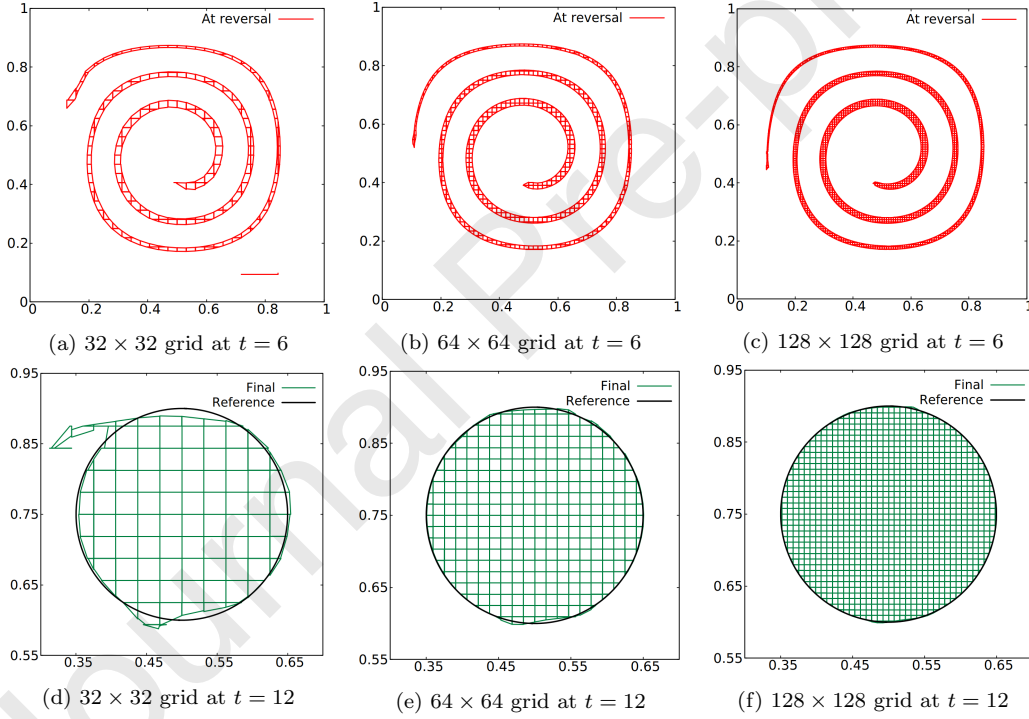
Figure 17: Reversible vortex test case using $T = 12$ for 32×32, 64×64, 128×128 grids. Top row of figures shows the maximum deformation. Bottom row of figures shows the final interface

$$f(t) = \begin{cases} 1 & 0 \le t < T_{max} - t_\epsilon/2 \\ \cos\left(\frac{\pi(t - T_{max} + t_\epsilon/2)}{t_\epsilon}\right) & T_{max} - t_\epsilon/2 \le t \le T_{max} + t_\epsilon/2 \\ -1 & T_{max} + t_\epsilon/2 < t \le 2T_{max} \end{cases} \quad (16)$$

26

477 At $T_{max} = 0.8$, time at maximum deformation, the flow is reversed. The flow
478 is reversed smoothly during a transition period of $t_\epsilon = 0.1$.

479   This test case provides a good insight into the filamentary formation of
480 materials as the filament tip is leading as opposed to trailing in the previous
481 benchmark. For the base grid, 32×32, the number of iterations is set to
482 $n_{it} = 160$ for the entire simulation and $\Delta t = 0.01$. The number of itera-
483 tions is increased proportionally with the mesh and therefore Δt is decreased
484 proportionally with the mesh.

485   The dynamic test is performed for different grids from 32×32 to 256×256
486 using a filamentary method. As the mesh is refined, this approach becomes
487 less relevant. The symmetric difference error is compared with [20] despite
488 an AMR capability being used in that paper. In addition, details of mass
489 conversation and runtime are given in Table 5. Fig. 18 shows the maximum
490 deformation and final reconstruction for 32×32, 64×64, 128×128 grids,
491 respectively. It can be seen that coarser meshes lead to larger error in re-
492 construction. In addition, the method exhibits some diffusion in the sense
493 of "floating" elements. These "floating" elements could be attenuated with
494 a higher tolerance in available cell volume fraction. Lower volume fraction
495 tends to create long and thin polygons, hence a larger error in reconstruction.
496 The lower bound of volume fraction available in a cell is set to 10^{-5} in our
497 model, compared to 10^{-8} in most comparative studies. We note that both
498 maximum deformation and final reconstruction show a symmetric left-right
499 deformation. As the tip of the filament gets thinner, even the filamentary ap-
500 proach cannot reconstruct the structure accurately. This leads to a shrinked
501 filament structure. When the grid is refined, the tip of the filaments are well-
502 defined and the final solution shows acceptable errors. The mass difference
503 is acceptable, bearing in mind the choice of only one round of redistribution.
504 In terms of runtime, the performance is compared with AMR [20] which uses
505 fewer cells than in this paper. The order of convergence of the solution shows
506 a remarkable performance compared to methods described in other papers.

507 *4.6. Benchmark: Rotating filament*

508   The rotating filament benchmark is a test case where a thin rectangle is
509 advected anti-clockwise in a rigid body rotation motion. The velocity field
510 is the same as in Sec. 4.2 and is given in Eq. (13). The rectangle is centered
511 at $(0.505, 0.75)$ in a unit domain. Its initial width is $w = 0.006$ and height is
512 $h = 0.3$. For a coarse mesh, here a 100×100 grid, the initial condition may

27

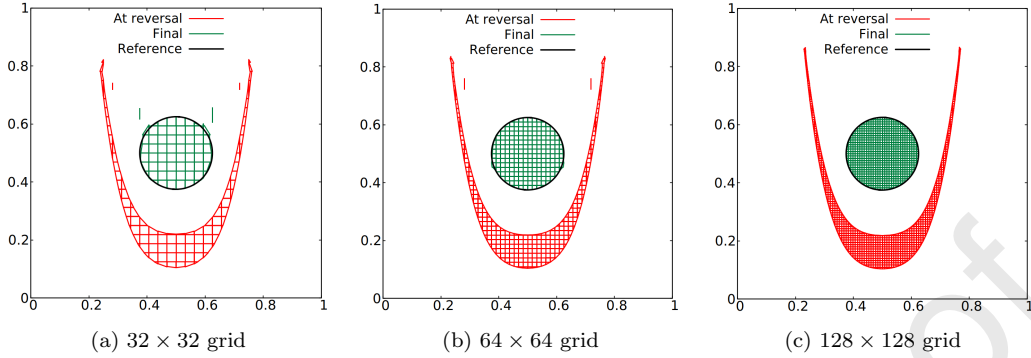(a) 32×32 grid   (b) 64×64 grid   (c) 128×128 grid

Figure 18: Intermediate and final reconstruction for the droplet flow test case for different mesh sizes. Red depicts the maximum deformation before reversal. Green depicts the final reconstruction. The black outline is the reference circle.

Table 5: Symmetric difference error, order of convergence, mass difference and runtime for the droplet flow test case at final reconstruction compared to reference papers.

Mesh size	32	64	128	256
E_{sym} in [20]	2.48×10^{-3}	6.37×10^{-4}	2.96×10^{-4}	-
Order of convergence	-	1.96	1.10	-
Runtime (s)	191.3	529.3	940.4	-
E_{sym}	1.71×10^{-3}	7.36×10^{-4}	1.26×10^{-4}	5.09×10^{-5}
Order of convergence	-	1.21	2.54	1.30
Mass difference	-1.16×10^{-9}	-1.07×10^{-7}	-4.49×10^{-11}	9.31×10^{-12}
Runtime (s)	3	9	29	166

already contain a filament structure. The corresponding number of iterations is set to $n_{it} = 300$ and $\Delta t = 2\pi/n_{it}$.

This benchmark can only be tested with a filament enabled approach on such coarse meshes. Indeed, even with a 200×200 grid, the filament body is subject to under-resolved filamentary structures. Fig. 19 shows the rotating filament at different stages of the full body rotation. The filament body is well reconstructed. However, both ends of the filament show cross-stream diffusion because the MOF method cannot reconstruct sharp edges accurately. In addition, the filament height is shortened due to the reconstruction error. The filament shortening matches with the height shown in [20]. The zoom on the top left of the figure highlights both shortening of the filament and cross-stream diffusion compared to the reference rectangle outlined in black.
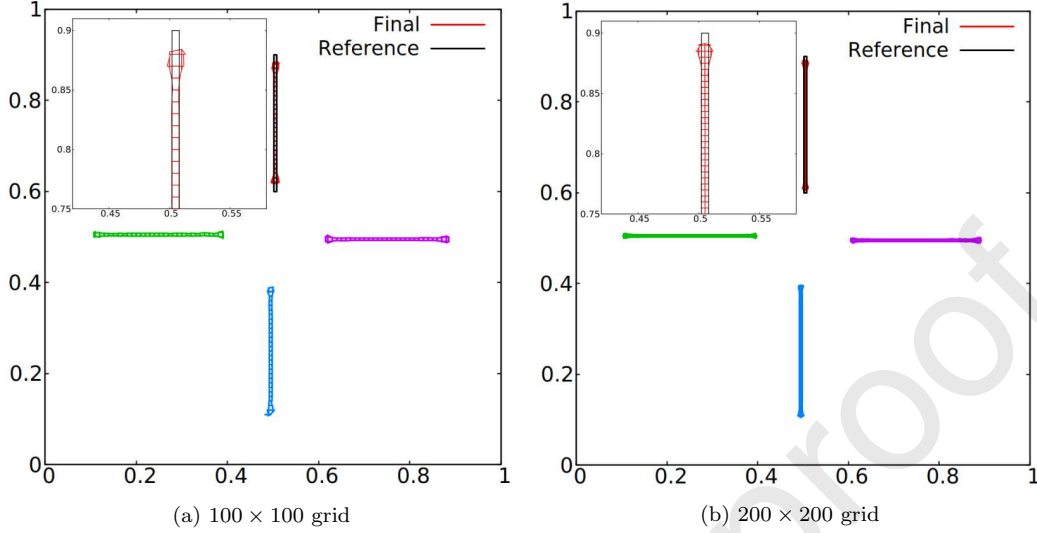
28

Figure 19: Solution of rigid body rotation for the rotating filament. Green depicts a quarter of rotation. Blue half rotation. Purple three quarter of rotation. Red depicts a full rotation and final solution. The black outline depicts the reference interface.

4.7. Benchmark: S-shape

The S-Shape test case comprises a circle of radius $r = 0.25$ initialised in the centre of a unit domain. The associated velocity field is nonlinear and divergence free and given by

$$\mathbf{u}(x, y, t) = \begin{bmatrix} 0.25[(4x - 2) + (4y - 2)^3] \\ -0.25[(4y - 2) + (4x - 2)^3] \end{bmatrix} f(t) \qquad (17)$$

The advection process creates a highly deformed and thin structure which means the filamentary capability is also enabled here. The amplitude $f(t)$ is given in Eq. (16). However, in this benchmark problem the maximum deformation occurs at $T_{max} = 4$ and the smooth transition period is $t_\epsilon = 2$.

This case shows strong deformation and thin structures, mainly in the centre of the domain. A coarse mesh would struggle to reconstruct these structures. Indeed, for the 32×32 grid in Fig. 20, the central part may have three interfaces within a cell. Therefore, capping to three materials is a limiting factor, creating larger errors in reconstruction. Because of large reconstruction errors, several structures may merge and lead to different end results. The 64×64 grid is fine enough to have a maximum of two interfaces in a cell. The deformed interface shows an accurate representation at maximum deformation.
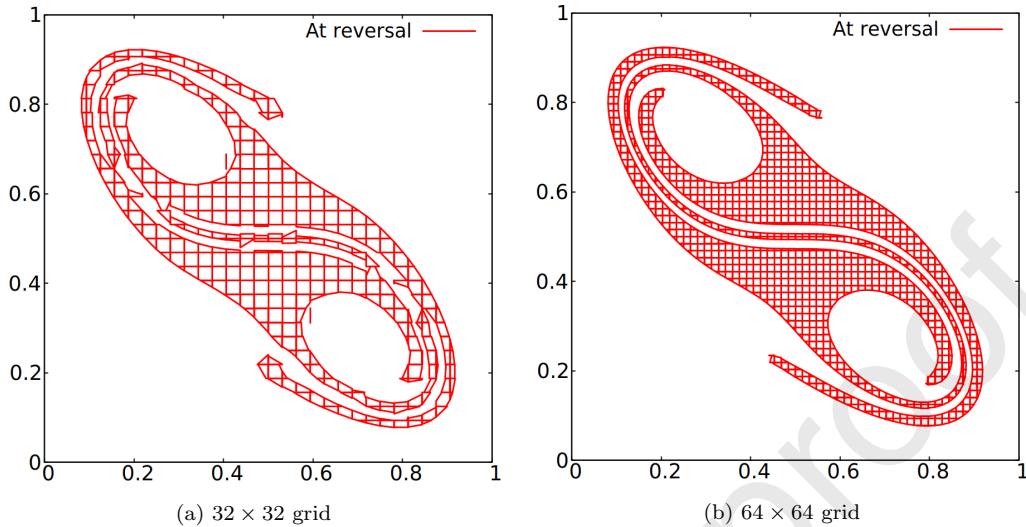
29

(a) 32×32 grid   (b) 64×64 grid

Figure 20: Maximum deformation for the S-shape benchmark.

5. Conclusions

In this paper, a new MOF method with a symmetric multi-material approach has been presented where thin structures are resolved using a filament approach for a fixed coarse mesh. A novel robust approach to solve the optimisation is proposed using a bisection method. No initial condition or parameters are necessary and the global minimum can be always found. A Lagrangian backtracking approach offers no limitation on the CFL number when advecting materials. Solving under-resolved filaments inherently involves a higher computational cost, which is reduced by choosing to cap the number of conglomerates at three and using a symmetric approach. As a result, almost quadratic order of convergence is achieved and the error converges as the grid is refined. However in complex and large material deformation, the limitation of this method is shown and the topology might not be well maintained at sharp edges.

This efficient approach is applied to several benchmark problems with different levels of deformation. Most of these benchmark problems are compared with different MOF approaches, filaments, AMR, CLSMOF and standard MOF. First, the Zalesak slotted disc does not exhibit any filament behavior, yet our approach shows good qualitative results. Other benchmarks such as the reversible vortex and the droplet flow case are tested for

30

large deformation highlighting the quality of reconstruction of filaments on coarse meshes. Finally, the rotating filament benchmark is presented, only applicable using filament reconstruction for such coarse grids. The limitation of our method is shown in the S-shape deformation benchmark. For most benchmarks, the error and runtime are comparable or better than other MOF methods. Furthermore, the accuracy in interface reconstruction is improved for large deformation. In addition, runtime has been decreased compared to most MOF methods.

The MOF method, like most interface capturing methods, diffuses when advecting sharp edges. In addition, the tip of filaments is not well-resolved regardless of the mesh resolution. In future work we would like to include the possibility to reconstruct four conglomerates within a cell while maintaining a high level of accuracy in reconstruction with an acceptable runtime. For a fixed coarse mesh, this may lead to an increased precision in thin layered filaments while reducing the natural diffusion of material. This approach could involve an optimised selection of which material to reconstruct. We would also like to use a selective adaptive mesh refinement method for complex and large deformation. Coupling our accurate MOF method with a fluid flow solver is our next priority with interest in both incompressible [29] and compressible [30] multiphase flows.

Acknowledgments

References

[1] R. Scardovelli, S. Zaleski, Direct numerical simulation of free-surface and interfacial flow, Annual Review of Fluid Mechanics 31 (1999) 567–603.

[2] G. Tryggvason, B. Bunner, A. Esmaeeli, D. Juric, N. Al-Rawahi, W. Tauber, J. Han, S. Nas, Y. J. Jan, A front-tracking method for

31

596 the computations of multiphase flow, Journal of Computational Physics
597 169 (2) (2001) 708–759.

598 [3] J. Li, An arbitrary Lagrangian Eulerian method for three-phase flows
599   with triple junction points, Journal of Computational Physics 251 (2013)
600   1–16.

601 [4] S. Leung, H. Zhao, A grid based particle method for moving interface
602   problems, Journal of Computational Physics 228 (8) (2009) 2993–3024.

603 [5] Y. Sato, B. Ničeno, A sharp-interface phase change model for a
604   mass-conservative interface tracking method, Journal of Computational
605   Physics 249 (2013) 127–161.

606 [6] M. Sussman, P. Smereka, S. Osher, A level set approach for computing
607   solutions to incompressible two-phase flow, Journal of Computational
608   physics 114 (1) (1994) 146–159.

609 [7] E. Olsson, G. Kreiss, A conservative level set method for two phase flow,
610   Journal of Computational Physics 210 (1) (2005) 225–246.

611 [8] R. Chiodi, O. Desjardins, A reformulation of the conservative level set
612   reinitialization equation for accurate and robust simulation of complex
613   multiphase flows, Journal of Computational Physics 343 (2017) 186–200.

614 [9] W. Doherty, T. N. Phillips, Z. Xie, A stabilised finite element framework
615   for viscoelastic multiphase flows using a conservative level-set method,
616   Journal of Computational Physics 477 (2023) 111936.

617 [10] C. W. Hirt, B. D. Nichols, Volume of fluid (VOF) method for the dynam-
618   ics of free boundaries, Journal of Computational Physics 39 (1) (1981)
619   201–225.

620 [11] M. Rudman, Volume-tracking methods for interfacial flow calculations,
621   International Journal for Numerical Methods in Fluids 24 (7) (1997)
622   671–691.

623 [12] J. López, J. Hernández, P. Gómez, F. Faura, A volume of fluid method
624   based on multidimensional advection and spline interface reconstruction,
625   Journal of Computational Physics 195 (2) (2004) 718–742.

32

[13] R. A. Remmerswaal, A. E. Veldman, Parabolic interface reconstruction for 2D volume of fluid methods, Journal of Computational Physics 469 (2022) 111473.

[14] J. Lopez, J. Hernandez, P. Gomez, F. Faura, An improved PLIC-VOF method for tracking thin fluid structures in incompressible two-phase flows, Journal of Computational Physics 208 (1) (2005) 51–74.

[15] M. Sussman, E. G. Puckett, A coupled level set and volume-of-fluid method for computing 3D and axisymmetric incompressible two-phase flows, Journal of Computational Physics 162 (2) (2000) 301–337.

[16] V. Dyadechko, M. Shashkov, Moment-of-fluid interface reconstruction, Los Alamos Report LA-UR-05-7571 (2005) 49.

[17] A. Lemoine, S. Glockner, J. Breil, Moment-of-fluid analytic reconstruction on 2D Cartesian grids, Journal of Computational Physics 328 (2017) 131–139.

[18] H. T. Ahn, M. Shashkov, Multi-material interface reconstruction on generalized polyhedral meshes, Journal of Computational Physics 226 (2) (2007) 2096–2132.

[19] V. Dyadechko, M. Shashkov, Reconstruction of multi-material interfaces from moment data, Journal of Computational Physics 227 (11) (2008) 5361–5384.

[20] M. Jemison, M. Sussman, M. Shashkov, Filament capturing with the multimaterial moment-of-fluid method, Journal of Computational Physics 285 (2015) 149–172.

[21] R. N. Hill, M. Shashkov, The symmetric moment-of-fluid interface reconstruction algorithm, Journal of Computational Physics 249 (2013) 180–184.

[22] H. T. Ahn, M. Shashkov, Adaptive moment-of-fluid method, Journal of Computational Physics 228 (8) (2009) 2792–2821.

[23] M. Jemison, E. Loch, M. Sussman, M. Shashkov, M. Arienti, M. Ohta, Y. Wang, A coupled level set-moment of fluid method for incompressible two-phase flows, Journal of Scientific Computing 54 (2) (2013) 454–491.

33

[24] A. A. Mukundan, T. Ménard, J. C. B. de Motta, A. Berlemont, A hybrid moment of fluid–level set framework for simulating primary atomization, Journal of Computational Physics 451 (2022) 110864.

[25] M. Cutforth, P. T. Barton, N. Nikiforakis, An efficient moment-of-fluid interface tracking method, Computers & Fluids 224 (2021) 104964.

[26] Z. Ye, M. Sussman, Y. Zhan, X. Zhao, A decision-tree based moment-of-fluid (DTMOF) method in 3D rectangular hexahedrons, arXiv preprint arXiv:2108.02533 (2021).

[27] Sutherland-hodgman polygon clipping algorithm, `https://rosettacode.org/wiki/Sutherland-Hodgman_polygon_clipping`.

[28] M. Shashkov, B. Wendroff, The repair paradigm and application to conservation laws, Journal of Computational Physics 198 (1) (2004) 265–277.

[29] Z. Xie, T. Stoesser, A three-dimensional Cartesian cut-cell/volume-of-fluid method for two-phase flows with moving bodies, Journal of Computational Physics 416 (2020) 109536.

[30] M. Jemison, M. Sussman, M. Arienti, Compressible, multiphase semi-implicit method with moment of fluid interface representation, Journal of Computational Physics 279 (2014) 182–217.

Declaration of interests

√ The authors declare that they have no known competing financial interests or personal relationships that could have appeared to influence the work reported in this paper.

☐The authors declare the following financial interests/personal relationships which may be considered as potential competing interests:

P.H.: Conceptualization, Methodology, Software, Data curation, Validation, Investigation, Visualization, Writing- Original draft preparation.

T.N.P.: Conceptualization, Methodology, Investigation, Writing- Reviewing and Editing.

Z.X.: Conceptualization, Methodology, Investigation, Writing- Reviewing and Editing, Funding acquisition.